Femtosecond Time Resolution in FM-AFM by Incorporation of a Ultrafast Pulsed Laser System

a Master Thesis in Nanophysics by

Raphael Pachlatko
raphael.pachlatko@stud.unibas.ch
University of Basel

Supervisor:
Prof. Dr. Ernst Meyer
University of Basel

Co-Supervisor:
Prof. Dr. Peter Grütter
McGill University, Montreal

July 17, 2017

Contents

1 Introduction

Atomic Force Microscopy (AFM) was invented in 1986 by Binnig, Quate and Gerber in order to record the topography of insulating samples [1]. In doing so, AFM expands on the possibilities offered by the previously invented Scanning Tunnelling Microscope (STM) by measuring tip-sample forces as opposed to tunnelling currents, which requires a conductive sample [2].

While various modes of AFM have since been conceived [3, 4], they all share common attributes. The central measuring unit consists of a conical tip with a radius of a few to few tens of nanometers which is attached to a cantilever, or occasionally another type of oscillator structure. Any change in the state of this oscillator which is due to an interaction of the tip with the sample or its surroundings is recorded, such as a change in oscillation amplitude, shift in resonance frequency, deflection or lateral torsion. The sample topography is recorded by scanning the tip across the sample surface while controlling and regulating varying parameters of its oscillation, such as amplitude or resonance frequency. The spatial resolution of the measured topography is dependent in part on the tip radius and the tip-sample separation, but is also dependent on other various parameters related to the sample itself and the feedback mechanism controlling the oscillator.

The AFM variant which is relevant for this experimental series, Frequency Modulated AFM (FM-AFM) was first introduced by Albrecht et al. in 1991, enabling the operation of AFM in vacuum [5]. FM-AFM observes the change in the resonance frequency of the cantilever due to tip-sample interactions, which enables ultimate performance conditions with high-Q cantilevers under ultra high vacuum.

To understand the motivation of this master thesis, it is advisable to review the work previously done on this topic, as this thesis is very much the continuation of previous work done by Z. Schumacher et al.

Within the larger setting of photovoltaics, it has always been a goal to measure charge carrier lifetime and other kinetic processes with both high spatial and temporal resolution, which has remained out of reach. In their publication , the authors present a general analysis of the lower limit for time resolution in AFM [6]. They suggest that the hard time resolution limit for AFM is given by the thermal limit [5] as opposed to mechanical parameters of the cantilever, as commonly assumed.

They demonstrate this by using a pump-probe approach with the cantilever as detector for the averaged signal. The advantage of this approach consists in its modularity; any excitation signal that can be measured may be used, provided in conjunction with a suitable experimental setup. In their case, two pulsed lasers are used as pump and probe signal, respectively, to measure the decay time of charge carriers (ca. 1ps) of a semiconductor. Their experimental setup, which

will form the basis for the experiments described in this thesis, is shown in figure 1.

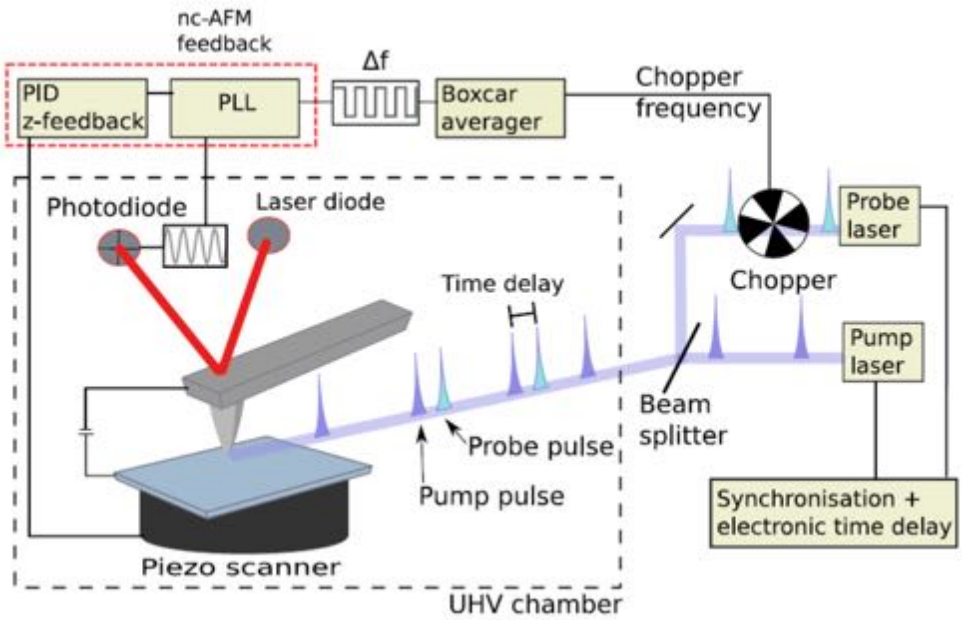

Figure 1: The experimental setup used by Z. Schumacher et al. [6] in their experiments.

While the setup used in our experiments is different in key areas, the operating principle remains the same: two laser pulses are focussed onto a spot below the cantilever with a variable relative delay. The first pulse to arrive "pumps" the sample to elicit a signal of variable nature, in the case of Schumacher et al., to generate a charge carrier. This signal possesses a certain lifetime. The second pulse arrives at the sample with a controllable temporal delay. By varying this temporal delay, be it via electronic or physical means, the "probe" pulse can temporally approach the timeframe where the "pump" signal has not decayed yet. Before reaching this regime, the "probe" pulse may, like the "pump" pulse, elicit a similar or identical signal. Once the delay time between the pump and probe pulse is sufficiently small to achieve an overlap of the pump signal's decay with

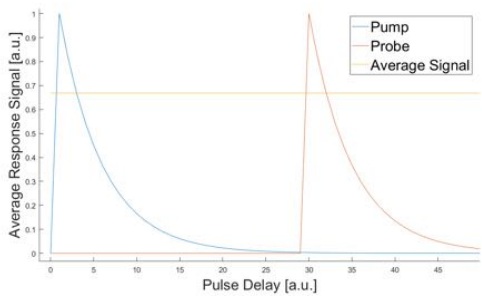

Figure 2: With sufficient delay, the individual pump/probe signals dont overlap and no difference in the average measured signal is achieved.

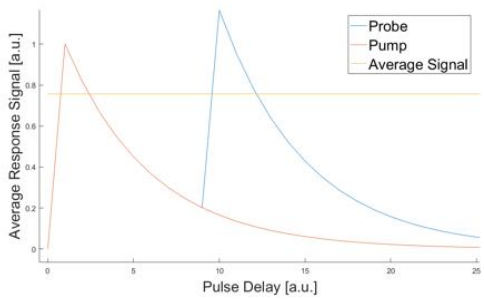

Figure 3: With beginning temporal overlap of the individual signals, the average measured signal changes.

the probe pulse's arrival, the average signal registered by the cantilever, in our case the frequency shift, will change. Two different pulse delays are sketched in figures 2 and 3, and the dependency of the average measured signal in proportion to the pulse delay is shown in figure 4.

A pulse overlap can also be used to have the pulses interfere with each other, opening up the possibility to measure interferometric autocorrelation using a suitable sample.

While the pump-probe approach requires that the characteristic lifetime of the measured signal is longer than the pump and probe pulses, in practice this is rarely an issue.

Schumacher et al. made use of a 780 nm NIR laser and a tunable visible laser which was delayed electronically. This thesis aims to modify the laser setup used by Schumacher et al. to use only one laser for both the probe and pump pulses. Specifically, here we aim to make exclusive use of the 780 nm NIR pulse laser for all measurements. This requires the splitting and controlled physical delay of an existing beampath where previously two lasers and beampaths were used. Doing this allows the measurement of fast phenomena, as the previous setup suffered from phase jitters exceeding 100 fs between the two different lasers, a problem which is eliminated by using only one laser.

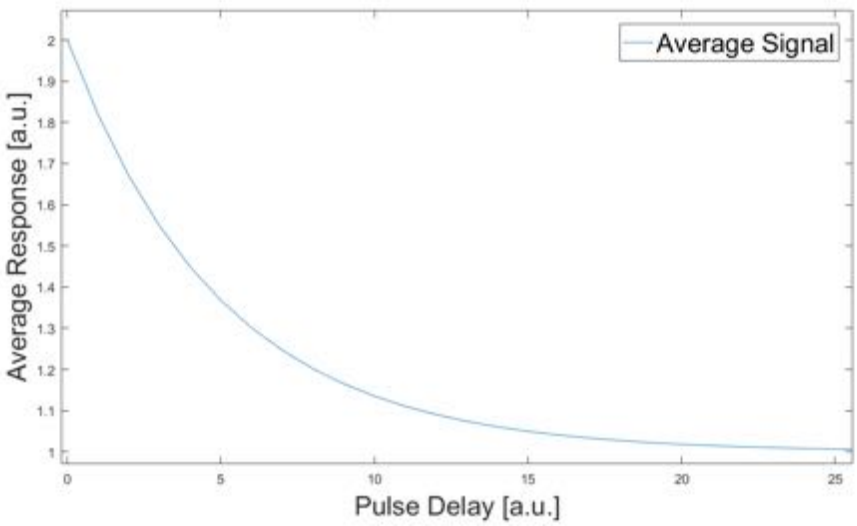

Figure 4: The average signal registered by the cantilever in relation to pulse delay. Note that the figures shown are conceptual and their specific signal dependencies reflect the specific case measured by Schumacher et al. [6].

This approach is also favorable since it uses only one laser for the pump and probe pulse, which also opens up the possibility of performing interferometric autocorrelation directly on a suitable sample in addition to classical pump-probe measurements. In order to monitor the delay between pump and probe pulses and to be able to characterize the laser pulse's shape, an

optical intensity autocorrelator is added to the laser system. The ultimate goal of this thesis consists in demonstrating that while the hard temporal resolution limit for AFM is given by the thermal limit, the detection limit for charge carrier lifetime and similar phenomena is given by the laser's pulse width, or more broadly, by the pump/probe signal's own duration.

2 Experimental Methods

The following sections will elaborate upon the experimental methods utilized in the experiments, namely Non-Contact Atomic Force Microscopy (nc-AFM) as well as Optical Intensity Autocorrelation.

2.1 Atomic Force Microscopy and Non-Contact Atomic Force Microscopy

With the invention of the Scanning Tunnelling Microscope in 1982 by Binnig and Rohrer [2], surface science was provided with the capability to image conductive samples with atomic resolution, and in 1986, with the invention of the Atomic Force Microscope by Binnig, Quate and Gerber [1], that capability was expanded to non-conductive samples.

An AFM generally consists of an etched, sharp tip (usually 10-20 nm) at the end of a cantilever which serves as force sensor. By approaching this tip to the sample and maintaining a constant force through a feedback loop while scanning the sample's topography with the tip, different measurement methods can be performed. The "contact mode", the first method to be developed, establishes mechanical contact with the sample and subsequently utilizes the repulsive force between the tip and sample to record the sample topography.

The "non-contact" mode on the other hand involves mechanically exciting the cantilever at or close to its resonance frequency using a piezoelectric vibration element which is incorporated in the holder where the cantilever chips are mounted for measurements. The deviation from the unperturbed oscillation due to tip-sample force is kept constant using the aforementioned feedback loop, which allows the tip to be approached at a constant tip-sample force without making direct physical contact. Figure 5 shows the generic setup of an AFM. Other detection methods are also available, however the method shown here is the most prevalent.

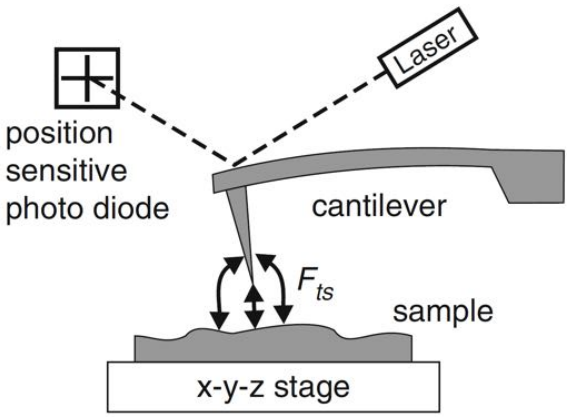

Figure 5: The basic working principle of an AFM, which consists of a laser reflecting off of the back of a cantilever into a position-sensitive quadrant photodiode and the actual sample mounted on a xyz stage driven by piezo motors [3].

This induced oscillation of the cantilever is described using its equation of motion as a damped driven harmonic oscillator, which assumes the cantilever tip is a point-mass spring [5, 3]

$$m\ddot{z} + \frac{m\omega_0}{Q}\dot{z} + kz = F_{ts} + F_0 cos(\omega_d t) \tag{2.1}$$

where k is the spring constant, m the specific mass of the cantilever, Q the quality factor, F_{ts} the tip-sample force, and F_0 and ω_d are the amplitude and frequency of the driving force of the piezo element. Under ideal conditions, the feedback loop compensates any potential energy loss and equation 2.1 can be expressed as [7, 8], since the damping term $\frac{m\omega_0}{Q}\dot{z}$ and $F_0\ cos(\omega_d t)$ can be neglected:

$$mz + k\ddot{z} = F_{ts} \tag{2.2}$$

f_0, the free resonance frequency of the cantilever, relates to ω_0, and depends on the spring constant of the cantilever and its effective mass m*, which also accounts for the cantilever's geometry [8]:

$$\omega_0 = 2\pi f_0 = \sqrt{\frac{k}{m^*}} \tag{2.3}$$

The precise spring constant for a rectangular cantilever can be calculated using

$$k = \frac{E_Y \omega t^3}{4L^3} \tag{2.4}$$

where E_Y is the Young's modulus and L is the cantilever length, ω is the width and t the height/thickness [9].

Tip-sample force is composed of numerous contributions, namely the van der Waals force and the electrostatic and magnetic forces as well as the chemical and repulsive forces. These forces and their short-range interactions with the cantilever tip are commonly described using the empirical Lennard-Jones potential as seen in figure 6 and described by equation 2.5 [10, 3]:

$$U_{LJ} = 4\epsilon[(\frac{\sigma_0}{r})^{12} - (\frac{\sigma_0}{r})^6] \tag{2.5}$$

where σ_0 is the characteristic distance where the intermolecular interactions amount to zero, r the tip-sample distance, and ϵ the potential well's depth. The larger distances of the Lennard-Jones potential are governed by attractive forces which culminate in the potential's minimum, where the repulsive forces start to become dominant. These forces result from overlapping electron clouds originating from the cantilever tip and sample, as well as the Pauli exclusion principle, and are usually limited in their range to ca. 5 Å, contributing to atomic contrast in high-resolution AFM images [11, 3].

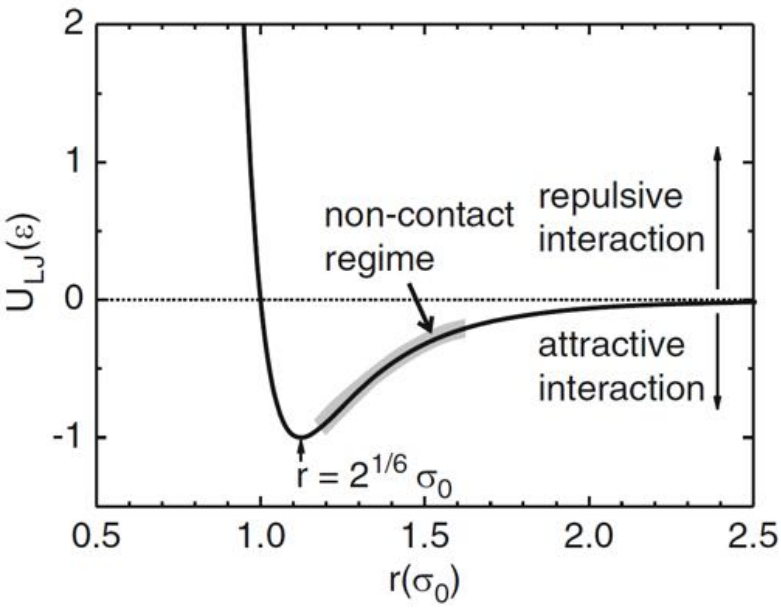

Figure 6: The Lennard-Jones potential describes standard tip-sample interaction forces at small distances. NC-AFM is performed in the non-contact regime [3].

2.2 Tip-Sample Interactions in Non-Contact AFM

As previously mentioned, the tip-sample forces in non-contact AFM are composed of three relevant components: van der Waals, electrostatic and chemical forces.

The **van der Waals** force is active in the attractive regime of the tip-sample interaction and comes into existence as a consequence of electric dipole fluctuations. In the case of AFM, the approximation of a sphere of radius R in front of an infinite sample plane is made. Thusly approximated, the force is described as follows [3]:

$$F_{vdW} = -\frac{HR}{6d^2} \tag{2.6}$$

where H is the Hamaker constant and d the shortest distance between the sample plane and the sphere. If the tip should approach the sample below the intermolecular distance a_0, F_{vdW} would be replaced by the adhesion force F_{adh}. For a stiff contact and small tip radii F_{adh} can be written as $F_{adh} = -4\pi R\gamma$, where γ is the surface energy [12]. For non-contact AFM and Electrostatic Force Microscopy (EFM) however, this relation is irrelevant, since any and all measurements for these methods take place in the non-contact regime as pictured in figure 6, which is governed by attractive forces.

The tip-sample force component most relevant for this Master thesis and for the measurements performed is the **electrostatic force F**$_{el}$. It arises as a consequence of various parameters such as different work functions, as well as potential surface charges on the sample. By considering the tip-sample system as a capacitor, F$_{el}$ can be expressed as [3]:

$$F_{el} = \frac{1}{2}\frac{\partial C}{\partial z}(V_{CPD} - V_{DC})^2 \tag{2.7}$$

where C is the Capacitance, V$_{DC}$ is the voltage applied to the tip and V$_{CPD}$ is the contact potential difference between sample and tip. F$_{el}$ will play a central role for the following measurements.

As the tip approaches the sample surface, tip-sample forces will shift the resonance curve of the cantilever. In the case of small cantilever amplitudes, one can approach this as a weakly perturbed harmonic oscillator. Thus the resonance shift can be described by the introduction of an effective spring constant [3, 4, 8].

$$k_{eff} = k - \frac{\partial F_{ts}}{\partial z} \tag{2.8}$$

The spring constant is modified by the force gradient $\frac{\partial F_{ts}}{\partial z}$ and as a consequence shifts the resonance curve, which is also known as **frequency shift**.

Assuming that the oscillation amplitude is small enough to remain within a linear, i.e. small force gradient, the frequency shift can be expressed as [4, 3, 8]

$$\Delta f_0 = -\frac{f_0}{2k}\frac{\partial F_{ts}}{\partial z} \tag{2.9}$$

This approximation illustrates that the frequency shift changes in proportion to the force gradient, and not the force itself directly. As mentioned, this approximation is only suitable for small oscillation amplitudes compared to the force gradients. For larger amplitudes, the cantilever may traverse different force regimes in the swing of one oscillation, where perturbation must be employed to obtain [4, 3]

$$\Delta f_0 = -\frac{f_0}{kA_0^2}\frac{1}{T_0}\int_0^{T_0} F_{ts}(d + A_0 + A_0 cos(2\pi f_0 t))A_0 cos(2\pi f_0 t)dt \tag{2.10}$$

where d is the sample distance, A_0 the oscillation amplitude, k the spring constant and f_0 the free resonance frequency.

2.3 FM-AFM Feedback Circuit

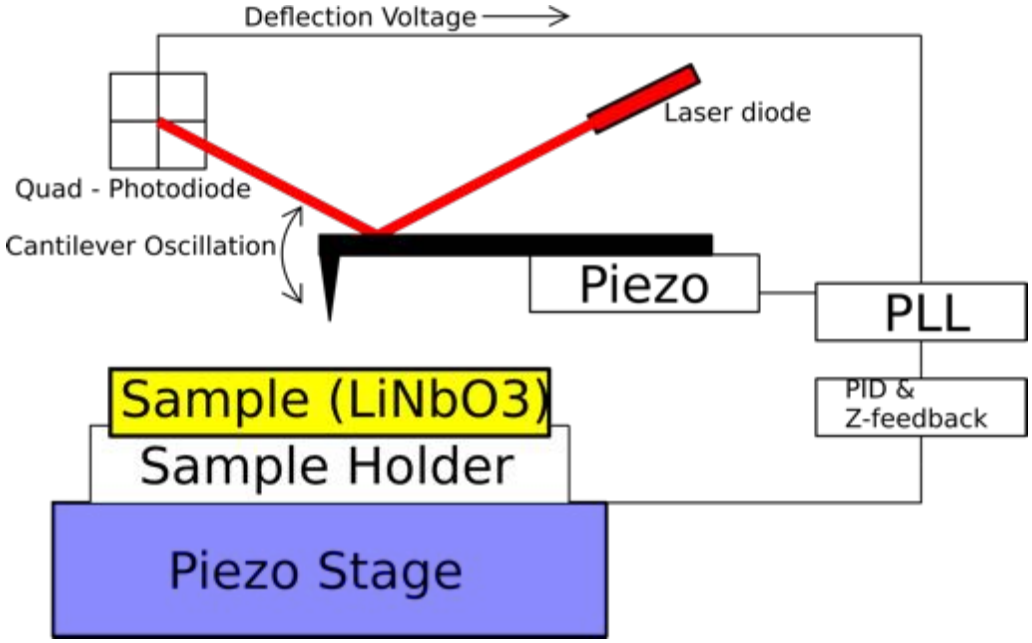

Figure 7: A block diagram of an AFM feedback loop for nc-AFM. The nc-AFM feedback loop consists of a PLL and PID controller in order to maintain a constant frequency shift with the cantilever.

As mentioned previously and shown in figure 7, the nc-AFM feedback loop uses a Proportional Integral Derivate (PID) controller and a Phase-Locked Loop (PLL) to maintain a constant frequency shift with the cantilever. The cantilever is driven by the piezo element and the piezo frequency in turn is regulated by the PLL. The z-feedback regulates the tip sample distance to maintain a constant frequency shift using a piezo-driven stage upon which the sample is placed. It is the readout from the z-feedback which eventually gives rise to a topographical image of the sample.

2.4 Intensity Autocorrelation and Pulse Characterization

The characterization of ultrashort laser pulses with a pulse length below the picosecond range is the current temporal resolution limit of ultrafast photodetectors [13]. Therefore, different methods need to be employed to characterize ultrashort laser pulses around and below 100 femtoseconds pulse length.

One such method is the optical second harmonic intensity autocorrelation.

Intensity autocorrelation essentially uses the ultrashort laser pulse to measure itself. The pulse in question is split into two independent beampaths which are delayed in relation to one another and subsequently reunited in a nonlinear optical material such as a crystal capable of second harmonic generation (SHG), also known as frequency doubling, which produces light at half the wavelength of the input beam.

Such a setup will only produce the characteristic second harmonic light if a pulse overlap is achieved. This second harmonic signal is measured against the variable pulse delay, yielding the so-called autocorrelation trace.

The intensity of the autocorrelation trace can be expressed as [14, 15, 16]

$$I_{AC}(\tau) \propto \int_{-\infty}^{\infty} |A(t)A(t-\tau)|^2 \, dt \tag{2.11}$$

$$\propto \int_{-\infty}^{\infty} |I(t)I(t-\tau)| dt \tag{2.12}$$

where τ is the time delay between the two pulses, $A(t)$ is the complex envelope of the input pulses and $I(t) = |A(t)|^2$ is the intensity. The intensity of the autocorrelation trace will thus be zero unless a partial or complete pulse overlap is achieved.

A generic setup for an intensity autocorrelator, shown in figure 8, consists of two beam splitters, an optical delay stage, a focussing lens, a nonlinear crystal capable of second harmonic generation (SHG) and a detector. Optionally, the setup can be refined with a shutter and an additional focussing lens behind the crystal.

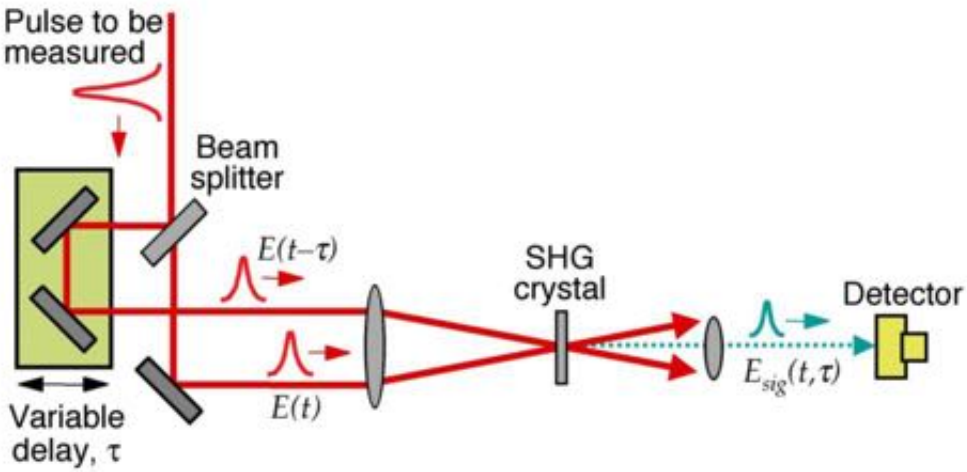

Figure 8: The generic setup for a non-collinear second harmonic intensity autocorrelator [14].

While the autocorrelation trace registered by the detector does not contain the full information about the input pulse, this information may be retrieved if the original pulse shape is known [15]. Such data can easily be retrieved for a specific laser system and is usually provided as part of quality assurance.

Assuming that the pulse shape has a Gaussian shape, its power can be expressed as

$$P(t) = e^{-\frac{t}{T}^2} \tag{2.13}$$

where P is the pulse's power in arbitrary units, t is time and T is the pulse-specific parameter. The pulse's Full Width at Half Maximum (FWHM) is $2\sqrt{ln2}T$.
In the case of an autocorrelation trace, the original pulse's FWHM can be extracted using a deconvolution factor, which relates the autocorrelation trace's FWHM to the original pulse's FWHM. For Gaussian pulses, this deconvolution factor is

$$\frac{t_p}{t_a} = 0.7071 \tag{2.14}$$

where t_p is the pulse FWHM and t_a is the autocorrelation trace FWHM [15].

3 Materials and Methods

This section will elaborate on the materials, methods and devices used for the experiments, namely the UHV AFM system as well as the NIR Laser setup and various additional modifications and customizations.

3.1 UHV AFM Setup

As mentioned previously, this Master Thesis is in many regards a continuation of previous projects and experiments conducted with the same system [7, 17, 6]. The basis for all experiments and modifications consisted of a JEOL 4500A UHV AFM which was modified with custom attachments. The system is outfitted with a load lock leading into a preparation chamber, which in turn leads into the measurement chamber, as shown in figure 9.

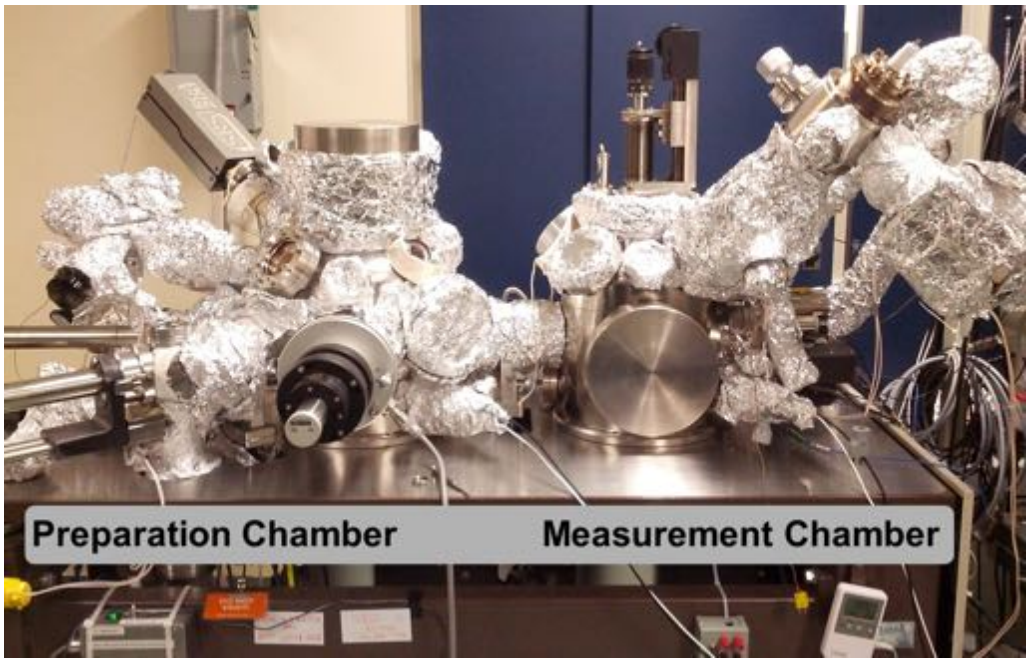

Figure 9: The UHV AFM system with the load lock visible to the left of the preparation chamber [7].

Depending on the amount of impurities present in the system's interior, it can maintain a vacuum of 10^{-10}-10^{-11} mbar using an ion pump (Satsuki SIP-300XH-T16) and a titanium sublimation pump (ULVAC PGT-3F) for each chamber. The load lock is outfitted with a turbo-molecular pump (Pfeiffer TMU261) to assist with initial pumpdown of the load lock with a regular rotary pump (Adixen 2010SD). This pump setup combined with the fast load lock bake time of roughly 6 hours allows for easy and relatively fast transfer of both AFM tips and samples. The transfers inside the system are handled with two magnetically coupled linear transfer arms, which is facilitated by a carousel mounted in the preparation chamber. The carousel can be rotated on 2 axes and translated on one axis to finely align with the transfer

arms and is capable of holding 3 sample holders and 1 tip holder. Further sample storage is installed in the measurement chamber with a capacity of an additional 3 samples. The entire system itself is mounted on an air-dampened anti-vibration table to minimize vibrational noise, furthermore the AFM stage itself is also spring loaded to allow for additional damping [7].

3.2 Femtosecond Pulsed Pump-Probe/Interferometric Autocorrelation Laser Setup

The laser setup for the experiments consisted of a FemtoFiber Pro near infrared (NIR) Erbium-based pulsed fiber laser made by Toptica Photonics. The laser can be operated at 1560 nm wavelength with a power of $>$ 350 mW or alternatively at 780 nm with a power of $>$ 140 mW using an internal second harmonic generation system. The individual pulse width of a single laser pulse is 94 fs for both modes with a repetition rate of 80 MHz. This experiment series exclusively made use of the 780 nm mode.

Unlike the previous setup [6, 17], the goal of this thesis was to incorporate an interferometric autocorrelation laser setup which made use of only one source, namely the temporally "shorter" NIR laser (figure 10). This carries the intrinsic advantage that the pulses are identical, which facilitates data acquisition, as will be evident by examining the results. Another change which must be observed is that the beams can no longer be delayed electronically, since they share their source. Instead, the delay is achieved by using a physical delay stage (Thorlabs DDS220) with a retroreflector (Edmund Optics # 46-183) which allows one of the beampaths to be modified in its length, therefore delaying it in respect to the unaltered beam. The delay stage has a total driving range of 220 mm, which is doubled for the effective beampath, resulting in 440 mm of physical delay and 1.467 ns of temporal delay. A technical sketch of the laser setup is shown in figure 11 to clarify the relative positions of the individual elements of the laser setup.

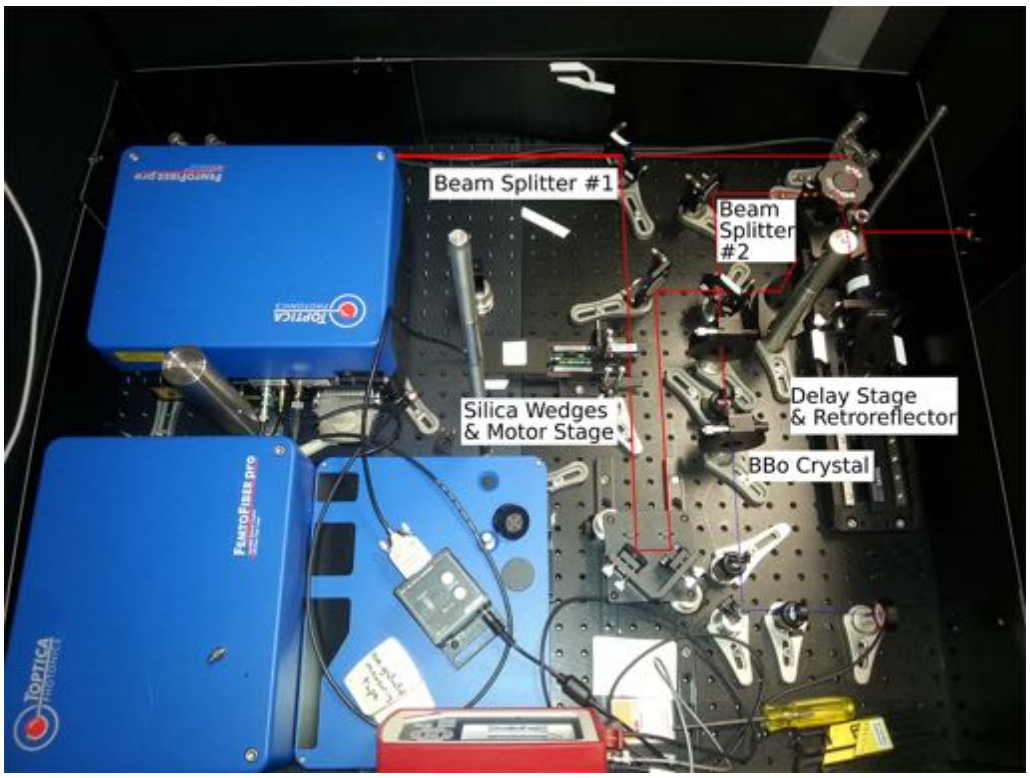

Figure 10: The final laser setup. Note the use of beam splitters to divide the source beam into two independently delayed beampaths, as well as the noncollinear beampaths after the second beam splitter. The $\lambda/2$ waveplate is marked in the schematic.

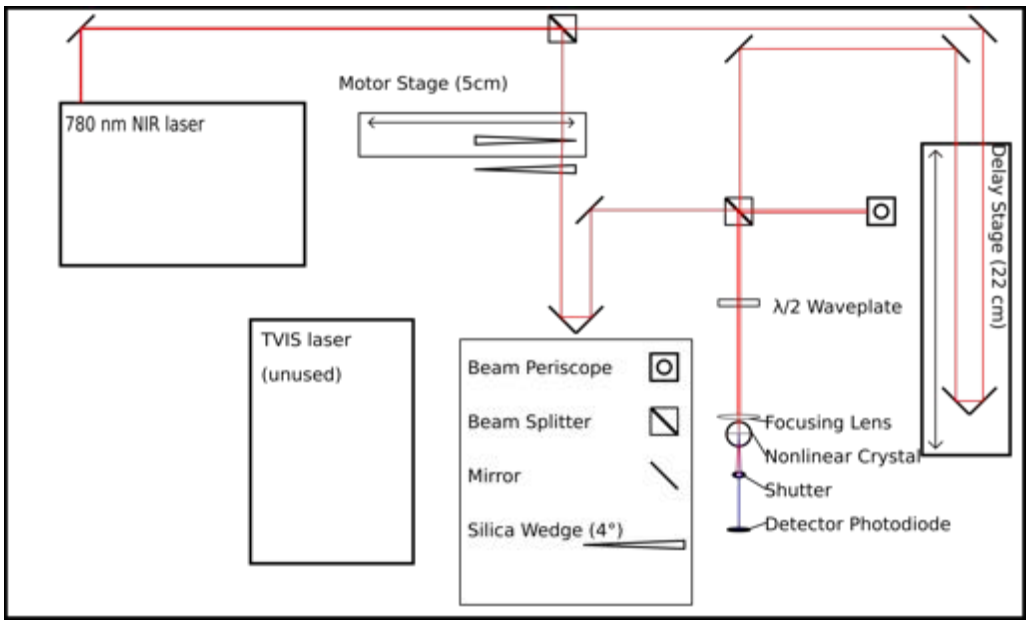

Figure 11: The laser setup in schematic form. Note the second motor stage with one of the two silica wedges mounted as a fine delay as well as the $\lambda/2$ waveplate.

In order to obtain the two necessary beampaths from a single source, two 50:50 beam splitters for P-polarized light were used (UFBS5050, Thorlabs) to split and reunite the beampaths. The

P-designation of the beam splitters refers to the polarization of the incident beam relative to the plane of incidence, in this case **parallel**, which corresponds to the laser's **horizontal** polarization. For reasons elaborated in section 3.3, the beampaths were not reunited in a collinear fashion after the second beam splitter, and instead were left to propagate parallel to each other. Furthermore, a $\lambda/2$ waveplate (WPH05M-808, Thorlabs) was employed in front of the autocorrelator setup as well as the beampath leading into the measurement chamber in order to rotate the laser polarization 90° into a vertical polarization and a P-incidence, respectively. Lastly, as will be explained in section 3.7, the retroreflector delay stage was supplemented with two silica wedges and an additional motor stage to allow for additional delay fine-tuning.

3.3 Autocorrelator Setup

In order to precisely determine and fine-tune the temporal delay between the pulses, it was necessary to explore the options of precise pulse characterization. Optical intensity autocorrelation, as mentioned previously, is a suitable and easily applicable method for pulse characterization [13, 14, 15, 16]. For this experiment, it was decided to use a nonlinear Barium Borate Crystal (BBo) with a noncollinear setup. Barium Borate has been used previously to generate second harmonic signals and also perform intensity autocorrelation, mostly in noncollinear setups [13, 18, 19, 20]. While the noncollinear setup has downsides in regards to the laser alignment into the UHV measurement chamber, it optimizes the quality of the autocorrelation trace which is obtained from the nonlinear crystal. As displayed in figures 10 and 11, the noncollinear beams are focussed into a ultrathin (<100μm) BBo crystal at an optimal angle[1] and polarization, and if a temporal overlap is achieved, a second harmonic autocorrelation trace will be produced by the crystal. This trace is geometrically located between the two source beams and can be isolated, in this case by using an iris aperture and a dichroic mirror. The aperture is

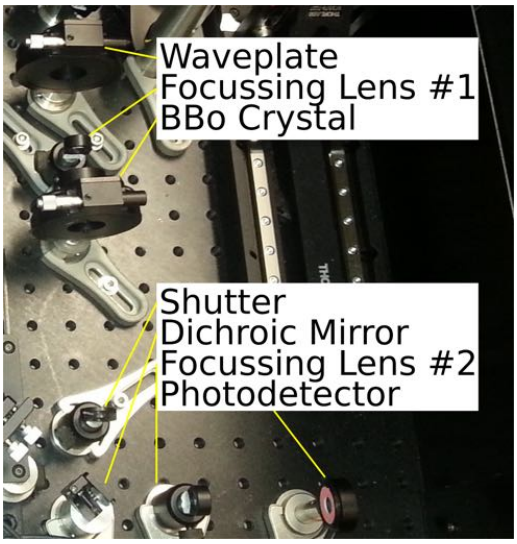

Figure 12: A closeup of the autocorrelator components. The shutter, dichroic mirror and the second focussing lens serve the purpose of filtering and aligning the signal trace.

[1]The optimal angle refers to the optimal angle of incidence for regular second harmonic generation. The angle was determined empirically by finding optimal angles for the two incident beams and subsequently orienting the crystal at the angle in between.

needed to block the largest part of the NIR beams (which diverge only at a small angle) since the dichroic mirror does not perfectly transmit infrared and thus would induce noise from the original beams. Subsequently, this trace is refocused using a lens and directed into a regular photodiode for detection (PM100D, Thorlabs). The refocusing of the trace is done for utility and ease of alignment, and is not necessary from a theoretical standpoint. A closeup of the setup can be seen in figure 12.

The motivation for the use of the waveplate in the setup is the fact that the nonlinear crystal has a specific incident angle required for second harmonic generation, and by extension, intensity autocorrelation [18, 20]. This angle varies depending on wavelength and can be experimentally determined for the purposes of this experimental series. Furthermore the crystal possesses a rotation axis which must be aligned to the incident beam's polarization, which is done by placing the crystal in a rotation mount as shown and aligning its axis until optimal intensities are achieved. The rotation of the crystal only had to be adjusted once, however the axial tilt had to be modified often to achieve optimal alignment.

As can be seen in figure 13, the BBo crystal is only a few millimeters in dimension. As the crystal needs to be tilted around its axis of rotation, which coincides with the polarization required from the input beams, it is also moved out of the beam path. Consequently, the crystal mount has its rotational plane horizontally aligned to allow quick manual adjustment. As this arrangement requires the rotational axis to be vertical, the beam polarization must be rotated to meet its alignment requirement. This was done by using a $\lambda/2$ waveplate which rotates the incident beams' polarization by 90°.

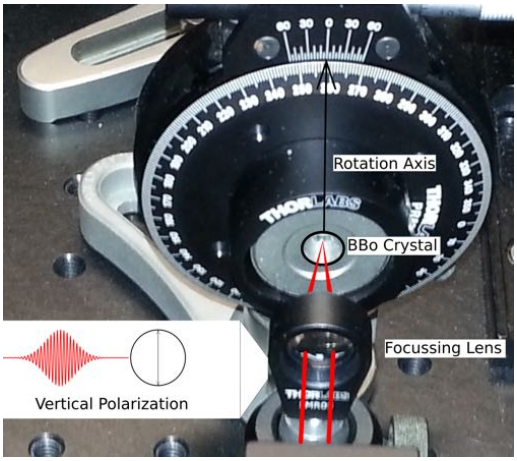

Figure 13: The BBo crystal fixed behind the focussing lens. Note that the waveplate is not visible in the picture, however the laser polarization has been modified to a vertical alignment.

3.4 Integration of Laser Setup with the UHV AFM Setup

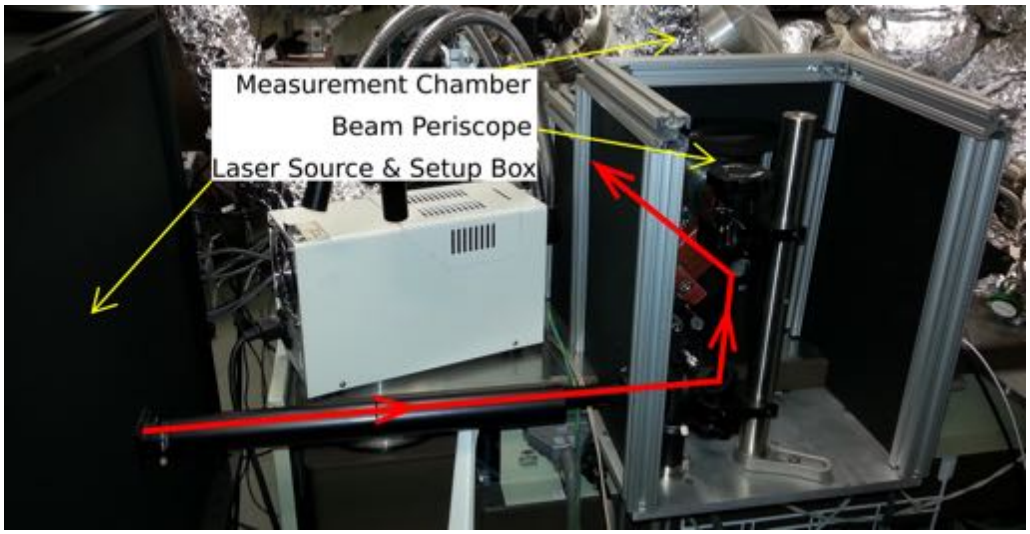

Figure 14: An overview of the beampath as it leaves the laser box. The beams are guided through a beam tube into a second box containing the $\lambda/2$ waveplate, a second beam periscope and the focal lens. A closeup of this assembly can be seen in figure 15.

While the physical integration of the laser system with the AFM was done previously by Z. Schumacher [7], some adjustments had to be made to accommodate the modified laser system. Therefore, these adjustments as well as the details of the integration will be discussed briefly.

As seen in figure 10, the laser beams exit the delay setup by way of a lifting periscope and through an enclosed tube which leads to a second periscope assembly which is coupled to the AFM table itself, as shown in figure 15. The periscope assembly is preceded by a $\lambda/2$ waveplate to adjust the beam polarization, and redirects the beam through a focal lens which in turn focuses the beam into the main chamber through a mirror assay which will be discussed here. The base AFM system conferred several constraints onto the integration of the laser system. Firstly, the laser should not illuminate the cantilever or any other parts of the AFM to minimize thermal heating, however it should illuminate the spot right below the tip.

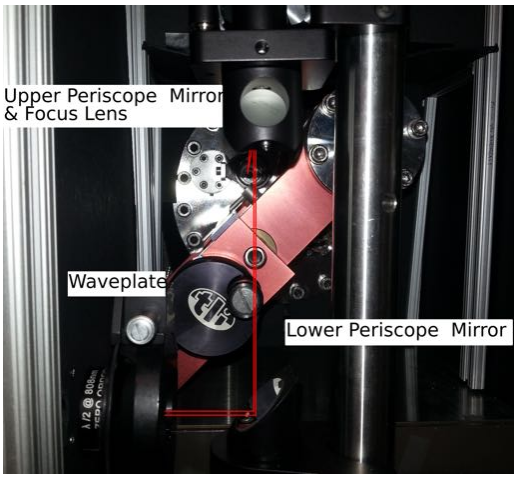

Figure 15: The second lifting periscope assembly, complete with the waveplate after the beam tube and the focal lens mounted right in front of the main chamber's window.

Secondly, the laser setup itself had to be isolated from the AFM table to decouple vibrations conferred to it from the AFM itself. Furthermore, the laser needed to illuminate the sample from a specific angle, right between the cantilever chip and the sample surface, leaving a total angle of 14°. In addition to this, the beams had to be aligned in a way so as not to interfere with the AFM's own detection laser, which is used to detect the cantilever deflection. Lastly, the cantilever's absolute position changes depending on the sample thickness and variations in mounting position. All this combined led to the incorporation of a movable mirror into the vacuum chamber to allow the beam to be adjusted precisely [7].

The mirror is a stick-slip piezo based ball mirror and can be seen in figure 16. The actual mirror is a 2 mm thick silver mirror glued to a steel sphere, which in turn rests on three sapphire hemispheres, which themselves are attached to piezo stacks. Additionally, the mirror is held down by a magnet which is place underneath the sphere in order to modulate the force transferred onto the sphere by the piezo stacks. The underlying idea of this design is the fact that the load, in this case the steel sphere with the mirror attached, will move and rotate along the piezo extensions if the movement is executed slowly, but will not move if the motion is done abruptly, hence the name "stick-slip".

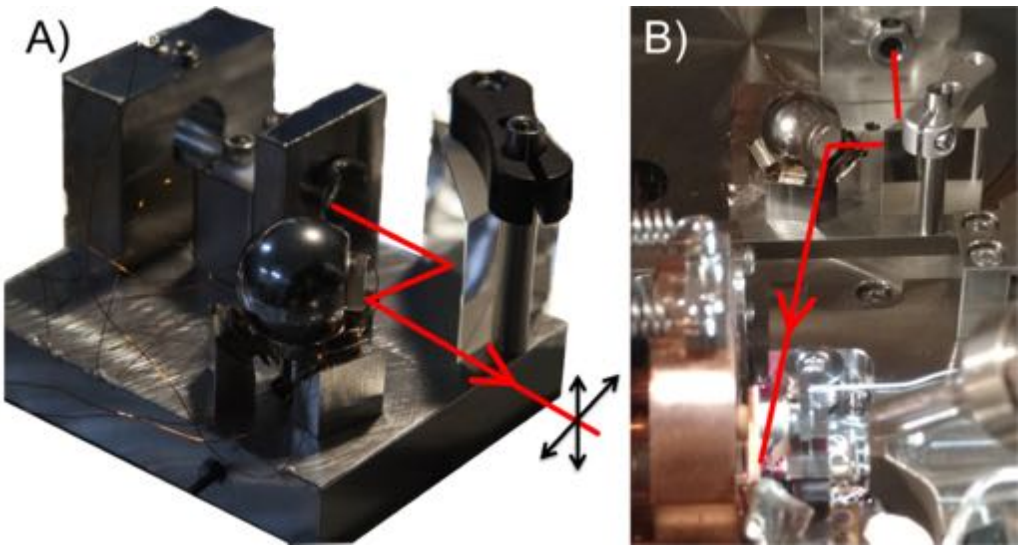

Figure 16: The stick-slip mirror incorporated with the larger static mirror before (A) and after (B) incorporation into the UHV chamber [7]. The red line denotes the beampath.

In order to achieve an alternating slow and fast movement of the piezo to effect a net movement in one direction, a sawtooth signal is applied to the piezos [7]. This "stick-slip" piezo design has previously seen use in UHV positioning applications [21].
This movable mirror design was then combined with a larger, static mirror to allow for the desired adjustment of the incident beam(s).

3.5 Optical Rectification and Illumination-Induced Polarization in Lithium Niobate

In order to allow for the measurement of an interferometric autocorrelation using AFM, a suitable sample had to be found which would produce a measurable signal proportional to the intensity of the incident light. A sample with the capability of optical rectification would fit such requirements. The prerequisite for the sample is that its crystal lattice is not centrosymmetric.

Optical rectification was first experimentally demonstrated by Bass et al. [23] and refers to the establishment of a DC polarization when an intense laser beam propagates through a nonlinear crystal. This phenomenon has found application in the generation of THz radiation pulses, first shown in 1965 by Berman et al. [24], and was widely expanded upon subsequently, with only a fraction mentioned here [25, 26, 27, 28, 29]. Franken et al. [30] established the scalar relationship between the electric susceptibility χ(E), the applied electric field E, and the polarization P:

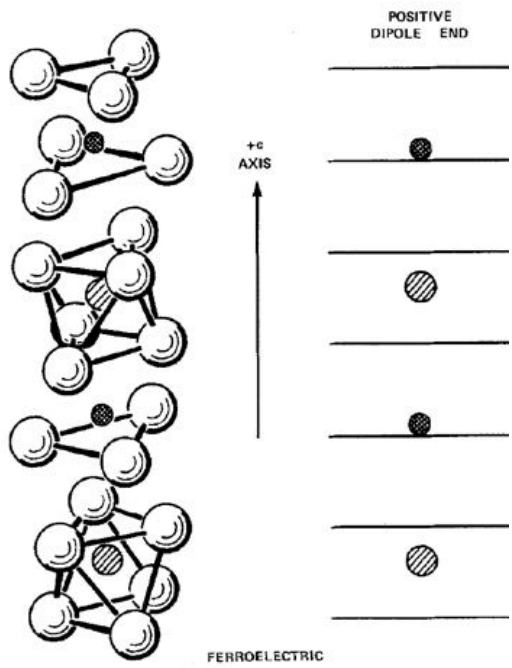

Figure 17: The positions of the lithium (dark) and niobium atoms (grey) in relation to the oxygen atoms (white). The crystal is pictured in the ferroelectric phase, which is the relevant phase for the experiments. Note the c-Axis, which denotes the direction of the DC polarization [22].

$$P = \chi(E)E \tag{3.1}$$

which states that the electric polarization of the target substrate is proportional to the electric field E, in this case the NIR laser. By expanding χ(E) in powers of the electric field E, one may describe the nonlinear optical properties of the material [31]:

$$P = (\chi_1 + \chi_2 E + \chi_3 E^2 + \chi_4 E^3 + ...)E \tag{3.2}$$

Since optical rectification is a second order nonlinear effect, it is described by $P_2^{nl} = \chi_2 E^2$ within the expansion. Consider an electric field which oscillates (much like the incident NIR laser) with $E = E_0\ cos(\omega t)$. In this specific case, the second order term consists of both a DC component $\chi_2 E_0^2/2$ and an oscillating component [31]

$$P_2^{nl} = \chi_2 E^2 = \chi_2 \frac{E_0^2}{2}(1 + cos(2\omega t)) \tag{3.3}$$

The DC polarization as described by eq.3.3 is the result of the rectification of the incident optical electric field by the χ_2 electric susceptibility of the target substrate. The oscillating term refers to second harmonic generation by the substrate [31]. Since this process is irrelevant for our experimental purposes, it will not be mentioned further.

Our choice for the nonlinear χ_2 material fell on Lithium Niobate ($LiNbO_3$), which has seen frequent use as a THz source [27, 26, 29, 25]. Its material properties and uses have been discussed [32, 22, 33], which provided the necessary details for sample selection.

Sanna et al. [32] state in their work that the crystal's c-axis, which is also referred to as z-axis, indicates the direction along which the DC polarization extends. As a consequence, the optimal sample to observe the DC polarization is a Z-cut $LiNbO_3$. Figure 17 shows the $LiNbO_3$ ferroelectric phase and the position of the respective atoms. It should be noted that in order to create this polarization, the incident optical electric field must have some component which oscillates along the polarization axis. Therefore, optimal polarization is obtained with a vertically polarized incident beam for this particular setup. This condition necessitates the use of the $\lambda/2$ waveplate as shown in figure 15 in order to rotate the polarization of the incident laser pulses into P-polarization, or vertical polarization. Figure 18 shows the final sample placement in the UHV AFM and its interaction with the system.

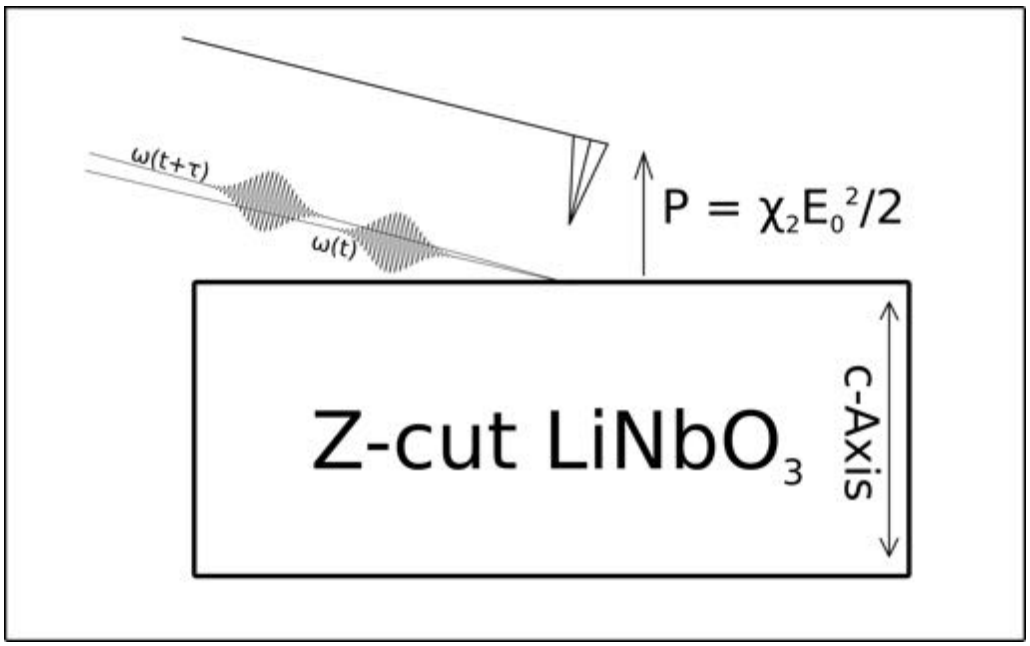

Figure 18: The placement of the $LiNbO_3$ sample. The c-Axis is perpendicular to the crystal surface, corresponding to a Z-cut. The incident laser pulses are P-polarized using a $\lambda/2$ waveplate shown previously. The resulting DC polarization manifests as an electric field which is proportional to the intensity of the incident electric field and which can be registered with the AFM tip.

3.6 Telescope-Mounted IR Camera for Precision Laser Alignment

As discussed in section 3.4, the means to align the laser beams onto the sample and below the cantilever tip were present. The incorporation of an IR-capable CCD camera and a modified webcam greatly facilitated the fine details of beam alignment. While the rough alignment had previously seen the use of a webcam which had its IR-filter removed to allow the observation of 780 nm laser light, the fine-tuning had no such options [7]. In the current setup, two beams simultaneously would incide onto the sample, and thus an optical reference was needed to ascertain that the individual beams were focussed into the same spot. To that end, a Jeol CCD camera which is part of the standard UHV AFM system was modified by again removing its IR filter to allow the observation of the NIR laser. This modified camera was then mounted on an optical telescope, which in turn was fixed in front of an observation window at the main chamber in a suitable angle to allow for direct line of sight onto both the sample and the cantilever chip. This setup allowed for direct observation of the cantilever chip, cantilever and the larger parts of the sample, which allowed the fine-tuning of the beam's alignment. It also allowed to remove any potential angular deviation which could be the result from minute changes in the system's overall position or temperature, and overall greatly streamlined beam alignment.

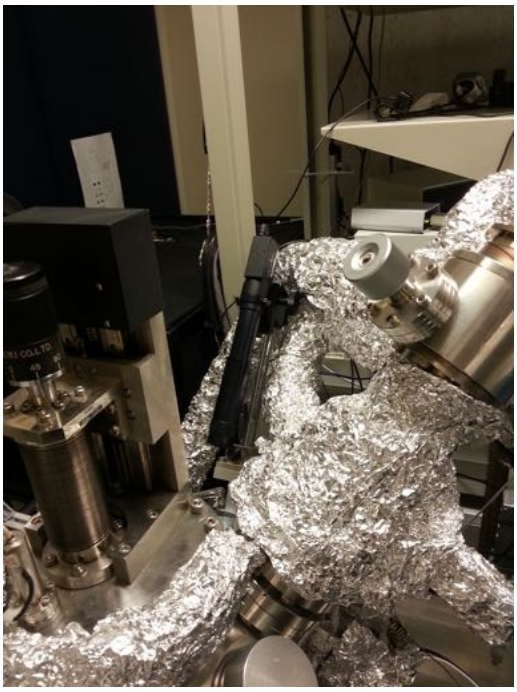

Figure 19: The IR CCD camera mounted on a telescope.

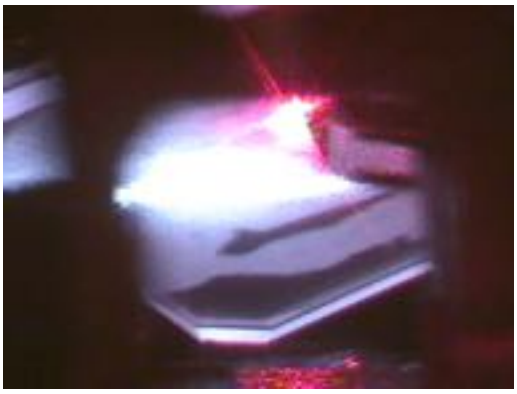

Figure 20: The laser beams focused into one spot next to the cantilever chip. The longitudinal shape of the beam spot is due to the incident angle of ca. 10°.

3.7 Incorporation of Silica Wedges

As announced in section 3.2, the laser setup initially only made use of the Thorlabs DDS220 delay stage to modify the beampaths. This had the drawback that the minimal achievable incremental movement of the stage intrinsically limited the temporal resolution of the measurements. This limit can be calculated as follows:

$$\Delta\tau_{min} = \frac{2d_{MIN}}{c} = \frac{2 * 0.1\mu m}{c} = 0.667fs \tag{3.4}$$

where c is the speed of light c = 2.99e^{8}m/s, d_{MIN} is the minimal achievable incremental movement, and $\Delta\tau_{MIN}$ is the temporal resolution limit.

In order to enhance the temporal resolution, a method involving a silica wedge pair was employed. By placing the wedges in the beam path in opposing orientations, as shown in figure 10 and 11, and by then subsequently moving one wedge perpendicularly to the beam path along its lateral axis using a delay stage (Zaber T-LSM025B-S), the effective material thickness through which the beam travels can be varied. The delay stage in question was exchanged with a replacement (Thorlabs MTS50B-Z8) during the experiments due to responsiveness issues. As a consequence, the beam is delayed proportionally to the change in wedge thickness, which can be stepped in much smaller increments than the linear delay stage it is mounted on. The concept of using wedge pairs has been previously explored; the temporal delay resulting from this setup can be calculated as follows [34]:

$$\Delta\tau_{min} = \frac{k * \Delta l(n-1)tan(\alpha)}{c} = 2e^{-17}s = 31.3as(Zaber)/6.5as(Thorlabs) \tag{3.5}$$

where $\Delta\tau$ is the temporal delay effected by the wedge's motion, Δl, which is 0.1905 μm for the Zaber delay stage and 50 nm for the Thorlabs replacement, respectively. N is the refractive index of the wedge material, and α is the angle of the wedge. K is a calibration factor used to equalize the measured pulse width to the coarse delay reference.

It should be noted that this calibration factor is used to account for irregularities in the fine delay by scaling the delay step values in the datasets to yield pulse widths resembling the coarse delay measurements. This is necessary since any deviation in wedge angle or refractive index of the wedge material results in a varying effective delay per actual motor distance driven. This is counteracted by scaling the pulse width measured with the silica wedges to a value measured by the coarse delay. This way, the coarse delay acts as a reference to ensure the fine delay is calibrated properly. The silica wedges used for the subsequent measurements had an angle of 4°. Using this additional delay mechanism, the minimal achievable temporal delay was improved by an order of magnitude to a few dozen attoseconds, as will be shown in section 4.2.

4 Ultrafast Interferometric Autocorrelation Measurements below the Intrinsic Pulse Width

This section will present and discuss the experiments involving the optical autocorrelator and the pump-probe/interferometric autocorrelation laser setup. The experiments will be treated separately, with the results of the optical autocorrelation placing an emphasis on pulse analysis and the interferometric autocorrelation experiment examining signal details. All experiments were conducted at a room temperature of 22 °C.

4.1 Optical Intensity Autocorrelation Measurements

As elaborated in section 3.3, an optical intensity autocorrelator was assembled in order to determine the precise location of the pulse overlap. In order to locate the "zero position" of the pulse overlap, the Thorlabs DDS220 delay stage (shown in figure 10 and 11) was stepped over its range while the intensity registered by the mounted photodiode was recorded.
The electronic readout and movement of the delay stage was coordinated using a custom-written LabView program.
The "zero position" was recognizable both by a peak in intensity, which is characteristic for intensity autocorrelation, and was also visible as a blue light trace (which really constitutes the second harmonic signal) upon examining the detection diode.

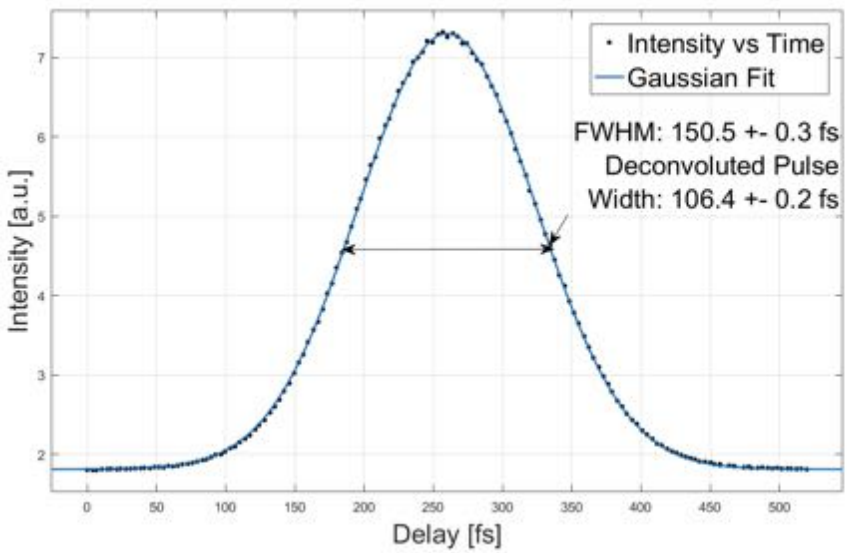

Figure 21: An intensity autocorrelation trace obtained by the coarse delay stage. A gaussian fit offers a suitable approximation of the pulse shape with a good R-square of 0.9999.

As mentioned previously, this delay stage served as a coarse delay, while the silica wedges in combination with a secondary delay stage, also shown in figure 10, were the fine delay due

to their significantly smaller stepping interval, as outlined in section 3.7. Figure 21 shows an intensity autocorrelation trace which was recorded using the coarse delay stage (DDS220). The trace exhibits a gaussian pulse shape with a FWHM pulse width of 150.5 fs. When the deconvolution factor (section 2.4) is applied however, the effective pulse width of 106.4 fs is revealed.

To relate this value to the pulse width of 94 fs given in section 3.2, it is necessary to consider that this pulse width was provided based on a Sech2 fit, which yields different pulse widths. To demonstrate this, the identical dataset from figure 21 was fitted using a Sech2 model. The resulting pulse width of 147.9 fs can be deconvoluted to an effective pulse width of 95.8 fs, which is much closer to the pulse width of 94 fs provided by the manufacturer. However, even a visual examination of the fit will reveal that a Sech2 model does not adequately approximate the pulse shape when compared to the gaussian model in figure 21. This is reinforced by a suboptimal R-square of 0.9983.

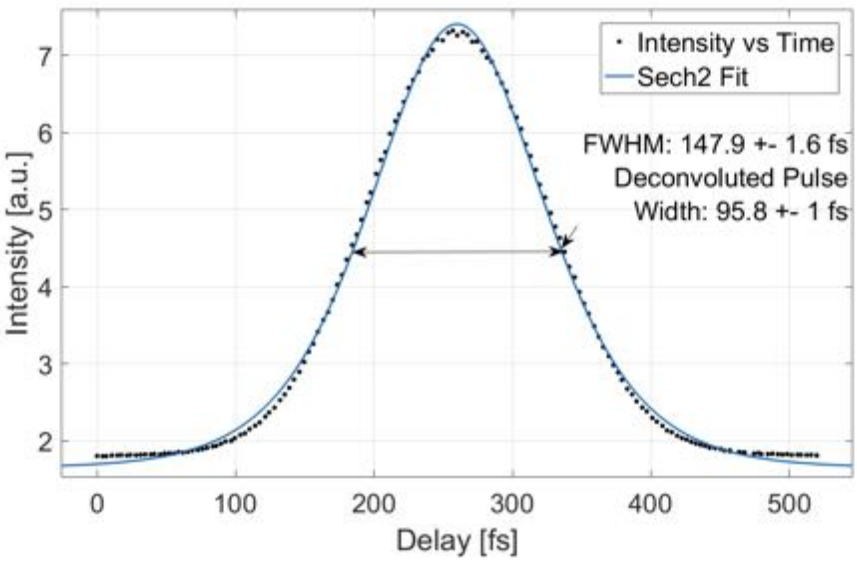

Figure 22: The identical dataset fitted with a Sech2 model. The pulse shape is visibly different from the fitted model.

In order to obtain better temporal resolution for the interferometric autocorrelation measurements, the delay stepping would be done using the fine delay with the silica wedges. To assure functionality and to calibrate the stage delay settings, optical intensity autocorrelations were also performed with the silica wedge pair acting as delay. Figures 24 and 23 show an autocorrelation trace recorded with this "fine delay".

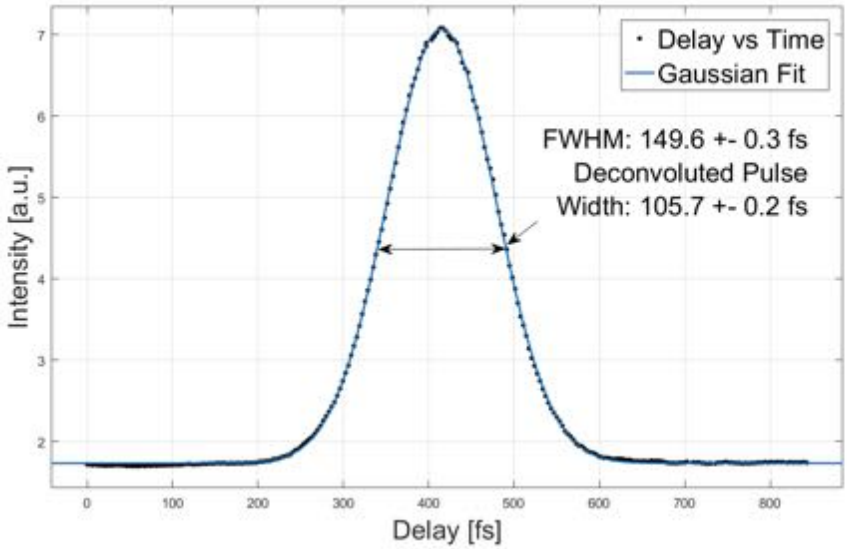

Figure 23: An intensity autocorrelation trace obtained using the silica wedge pair. A gaussian fit yields a pulse width practically identical with .

By applying equation 3.5 to the distance readout of the wedge motor stage, motor movement is converted into actual beampath modification. However, this equation assumes the values of parameters such as the wedge cut and refractive index of the material, which can deviate slightly. Such deviations have a large impact on the calculated beampath difference, and therefore it was necessary to calibrate the silica wedge pair. This was done by comparing the dataset recorded using the wedges with the one using the coarse delay stage, and then, using the coarse delay as a reference, applying the ratio of their FWHM as a correction factor. This ensures that the pulse widths obtained with the wedges correspond to the pulse widths obtained with the coarse delay.

Measurements with the fine delay are performed by driving the coarse delay to "zero" position at maximum pulse overlap and then subsequently stepping the fine delay around the position equilaterally.

The resulting autocorrelation trace exhibits a gaussian pulse shape with a pulse width of 149.6 fs, which yields a deconvoluted pulse width of 105.7 fs, which is practically identical with the value obtained by the coarse delay measurement, as is the intention for this calibration. Additionally, the gaussian fit corresponds visually with the dataset, reinforcing the gaussian pulse shape.

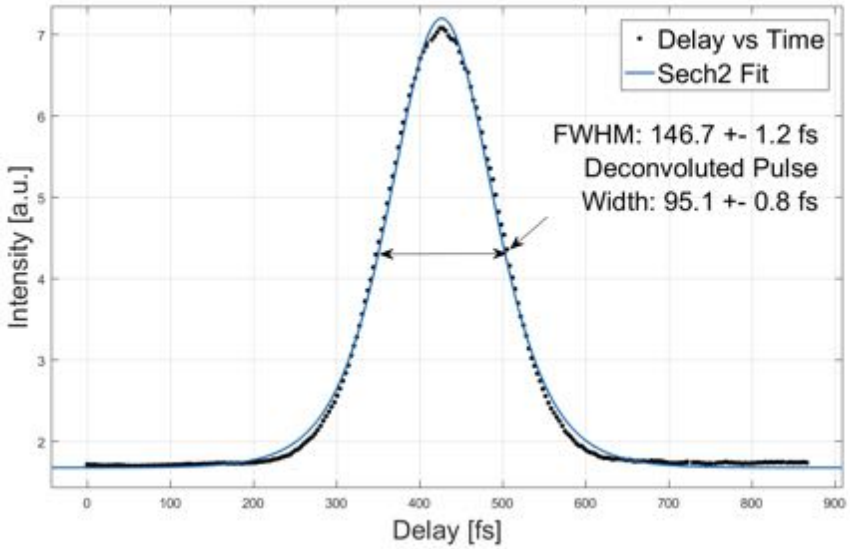

Figure 24: The same dataset fitted with a Sech2 model. Similarly to figure 22, the pulse shape visibly deviates from the dataset while also yielding a shorter pulse duration. The pulse duration obtained with the Sech2 model is well within the reference value of 94 fs given by the manufacturer.

Figure 24 shows the same dataset with a Sech2 model fitted to it. Similarly to the datasets recorded with the coarse delay, the Sech2 model does not visually conform with the dataset and yields a shorter pulse width. This shorter pulse width conforms well with the value provided by the manufacturer and as such validates the Sech2 fit as a means of reference with the provided reference.

It must be noted that the increased pulse width can be attributed to pulse dispersion which is introduced by the various optical components such as the beam splitters, silica wedges, focussing lenses and the $\lambda/2$ waveplate. This pulse dispersion is expected to increase as the beams propagate into the measurement chamber through more dispersive media.

4.2 Measuring Induced Polarization Gradients and Interferometric Autocorrelation Patterns on $LiNbO_3$

The core measurement of this Master Thesis consisted in the interferometric autocorrelation measurement conducted on Lithium Niobate. The aim of this measurement consisted in showing that temporal resolution in FM-AFM is not limited by the cantilever's mechanical parameters. As elaborated in section 3.5, Lithium Niobate fits the sample requirements for such a measurement.

The measurement was set up by directing the parallel beams into the measurement chamber by means of a beam periscope and a focal lens (figure 15), followed by a moveable stick-slip mirror assembly for fine alignment (figure 16).

Using these methods, the beams were focused onto one spot on the sample (figure 20), resulting in a configuration represented in figure 18.

The $LiNbO_3$ Z-cut crystal itself was fixed onto a sample holder and its edges were covered with silver paint to mitigate electrostatic charges. Additionally, the sample was inserted into the vacuum system without baking the loadlock, and by extension the sample. This was done to prevent a charge buildup due to the pyroelectric properties of the sample [35, 36, 37].

Once the beam alignment to the sample was completed, the cantilever tip was approached to the sample surface. This task turned out to be quite lengthy, as the sample was experiencing heating from the incident laser. This was readily noticeable, starting with a drift in resonance frequency which would always exceed 100 Hz in magnitude. The strong charging effects on the sample can be explained on one hand by its pyroelectric properties, on the other hand by its piezoelectric properties [38]. Figure 25 illustrates the extent in frequency drift and its timescale.

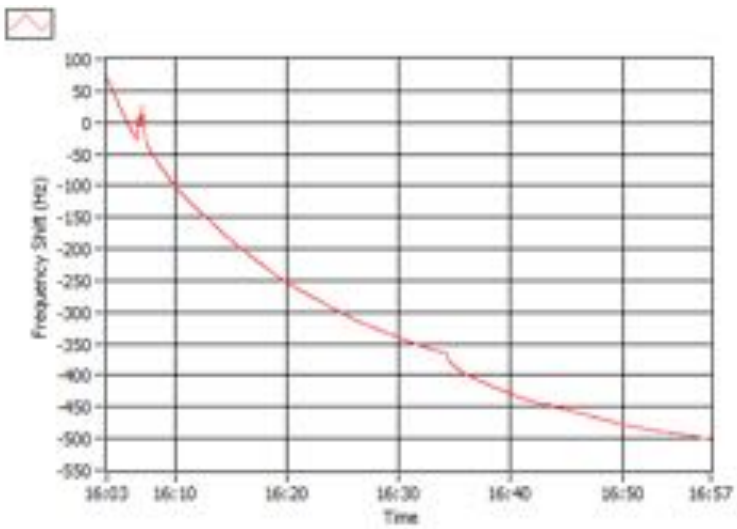

Figure 25: The drift of the resonance frequency of a cantilever in the vicinity of the $LiNbO_3$ sample.

The strong sample charge necessitated a relatively high setpoint of several hundred Hz to approach the sample satisfactorily. Once a stable setpoint was achieved, the interferometric autocorrelation measurement was initiated by stepping the silica wedge pair through the position of zero delay, identically to the optical intensity autocorrelation measurements discussed earlier. One dataset is shown in figure 26.

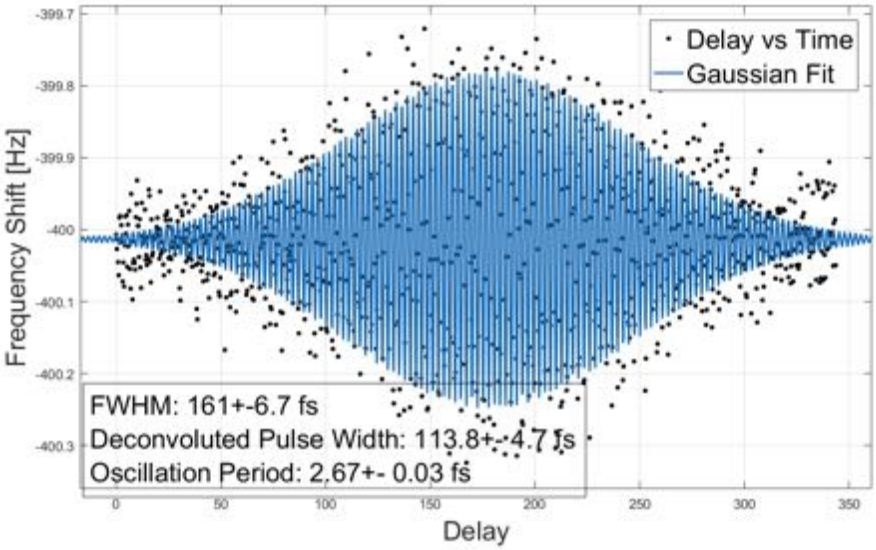

Figure 26: An interferometric autocorrelation trace recorded above $LiNbO_3$. Gradual stepping of the delay setting reveals a gaussian pulse with a width of 161 fs and an effective pulse width of 113.8 fs. The oscillations observable in the pulse shape stem from the interference between the pump and probe pulse. A closeup of the interferometric oscillations can be seen in figure 27.

The results from this interferometric autocorrelation lead to several conclusions. Firstly, the 2.67$\pm$0.03 fs oscillation period of the interferometric pattern closely corresponds to the laser's wavelength of 780 nm. Secondly, the fact that this interferometric pattern can be observed at all using a cantilever tip indicates that the degree of spatial resolution is sufficient not to average over several interferometric oscillations. As a sidenote it should be restated that the beam setup for this interferometric autocorrelation measurement is non-collinear, and therefore there is no large-scale phase coherence between the individual beams. While this reaffirms some degree of required spatial resolution of the tip, the interferometric pattern extends in dimension on the order of 10μm, therefore requiring only insignificant spatial resolution to resolve reasonably. Figure 27 shows a closeup on the interferometric pattern with an emphasis on the oscillation period.

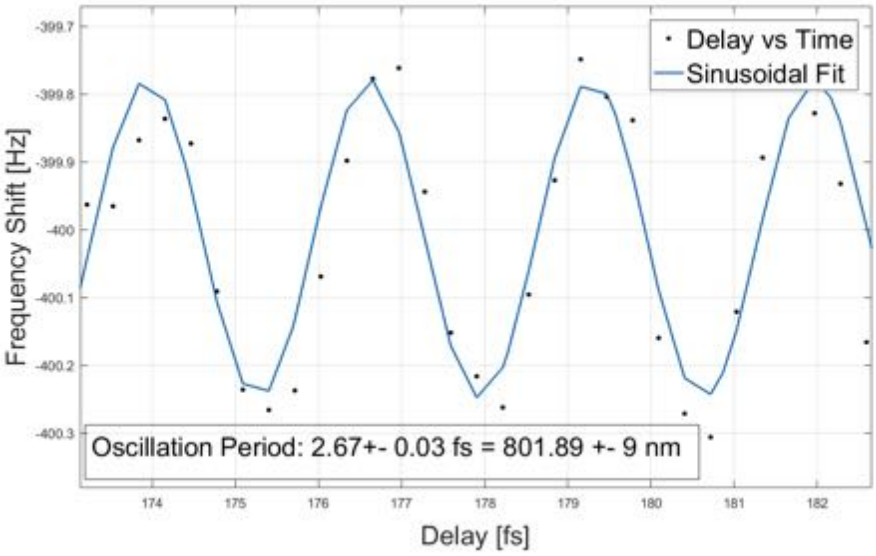

Figure 27: A closeup of the interferometric autocorrelation trace shown in figure 26. The oscillation period of 2.67 fs corresponds to a wavelength of 801.9 nm, which is slightly above the laser wavelength. This deviation can be due to the assumption of a constant wavelength, which disregards the spectral bandwidth of the laser. Similarly, potential chirp is not accounted for in the fit parameters.

The interferometric autocorrelation trace shown in figure 26 and 27 was accomplished with an active z-feedback. The reason why a tip lift was not executed was due to prohibitive drift during the measurement. This required the z-feedback to be responsive enough to compensate for the macroscopic drift, but slow enough to allow for the interferometric pattern to be recorded.
This restriction only applied for measurements which required an extended period of stability. It was attempted to resolve the autocorrelation trace by measuring small intervals, usually a single oscillation, by executing a tiplift, stepping the required distance, and then reapproach the sample to repeat the process. The individual segments would then be "stitched" together to form a complete autocorrelation trace. While this technique produced a nice resolution of individual oscillations, the concatenation of different datasets produced a result which possessed no higher quality than the continuous measurement with active z-feedback.
However, since the delay steps were minimized for the individual segments to maximize the resolution, these individual oscillation datasets demonstrate the minimal achievable delay setting with this particular setup of delay stages and wedge pair.

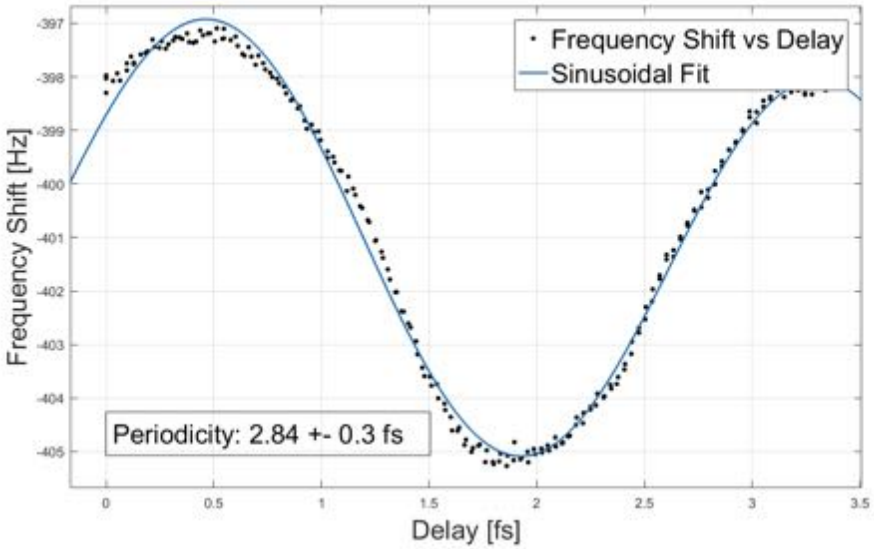

Figure 28: A single oscillation of the interferometric autocorrelation trace. The individual step size of the delay equates to 31.3 attoseconds of temporal delay.

The temporal resolution of the trace oscillations as shown in figure 28 represents the minimal delay setting that is achievable with the current setup. In comparison to the dataset shown in figure 26 and 27, which took several minutes to record, this measurement was in the time range of a minute. The periodicity of the oscillations here is however substantially higher, and does not correspond to the central wavelength of the laser. This can be explained on one hand by the laser's bandwidth, on the other by a possible chirp of the laser pulses. Lastly, the time frame spent recording a single oscilation was substantially longer than in the macroscopic trace measurement, and a tip lift was performed, which could leave the measurement vulnerable to small drift.

All these factors taken together may account for the increased periodicity and suboptimal fit, however the fact remains that a minimal incremental step size of 31.3 attoseconds was achieved.

5 Discussion

5.1 Optical Intensity Autocorrelation

The setup of an optical intensity autocorrelator served the purpose of characterizing the pulse shape of the pump-probe beams, as well as determining the physical location of the pulse overlap. Since the incorporation of the autocorrelator setup does not impede the beam-path leading to the UHV system, both the optical intensity autocorrelation and the pump-probe/interferometric autocorrelation measurement could be recorded simultaneously. In the present case however, this was prevented by the fact that both beampaths require the same waveplate be placed in them. Since only one waveplate was available during the time of the experiments, it was necessary to switch the waveplate between the two beampaths accordingly.
The optical intensity autocorrelation measurements revealed several things: firstly, it was shown that the pulse shape conforms well with a gaussian pulse shape, as opposed to a Sech2 shape as suggested by the manufacturer. Similarly, it was discovered that the pulse duration of 94 fs, fitted to a Sech2 model, was subject to pulse broadening due to material dispersion, if only slightly. The resulting pulse width of 95 fs was still within error in relation to the reference. Furthermore, it was noted that fitting the datasets with a gaussian model resulted in a more accurate representation of the pulse shape. However, the gaussian model would consistently yield larger pulse widths, therefore it must be kept in mind that the gaussian pulse width, while larger, is still representative of the "true" pulse width due to the gaussian shape of the pulse itself.
As described in section 3.2, the laser setup was fitted with two separate delay stages. The DDS220 delay stage acted as a coarse delay, performing the initial autocorrelation measurements to locate the pulse overlap and perform the first characterization of the pulse shape and duration. Subsequently, the fine delay, consisting of the silica wedge pair and a motor stage, would be used to resolve a second round of intensity autocorrelation measurements in order to ascertain its proper function and to calibrate the delay intervals of the fine delay using the coarse delay measurements as a reference, resulting in a conversion factor for the fine delay.
As a consequence, the comparison between the two datasets yielded a good agreement, with the Sech2 pulse width at 95.8±1 fs for the coarse and 95.1±0.8 fs for the fine delay. Accordingly, the gaussian pulse width of 106.4±0.2 fs for the coarse delay is close to the 105.7±0.2 fs of the fine delay.
In summary, the Sech2 fits verify the provided pulse width, albeit at the expense of fit accuracy, while the gaussian fits generally provide a larger pulse width, which is also more accurate, as both fitting error and visual inspection of the fits confirm.
This solidifies the statement that the NIR laser pulses possess a gaussian pulse shape and

also verifies the accuracy of the fine delay, which will be instrumental for the interferometric autocorrelation measurements discussed in the following section.

5.2 Interferometric Autocorrelation on $LiNbO_3$

Using the methods described in section 3.4, the laser beams were directed into the measurement chamber and focussed below the AFM cantilever. The interferometric autocorrelation measurements were executed by stepping the fine delay through the pulse overlap and recording the frequency shift with an active z-feedback. The resulting interferometric autocorrelation trace reveals a pulse length of 113.8±4.7 fs and interferometric oscillations with a periodicity of 2.67±0.03 fs, equating 801.89±9 nm, which just outside of the NIR laser's wavelength of 780 nm as well as its bandwidth.

The fact that this interferometric autocorrelation trace can be recorded at all leads to several conclusions. Firstly, the interferometric oscillations with a periodicity of 2.67 correspond closely to the NIR laser's wavelength. Secondly, the fact that the interferometric pattern is not averaged out by the cantilever tip infers a minimum of spatial resolution, although the required spatial resolution for this is within a few microns. Therefore this fact alone does not confirm nanometer-scale spatial resolution of the interferometric pattern, although the intrinsic spatial resolution of nc-AFM in itself is generally sufficient.

The broadened pulse width was to be expected given the amount of dispersive media through which the beams propagate before reaching the sample. The expected dispersion was estimated using [39]

$$\tau(L) = \tau_0 \sqrt{1 + (\frac{8\ a\ L\ ln(2)}{\tau_0^2})^2} \tag{5.1}$$

where τ_0 is the undispersed pulse width, a is the material-specific group velocity dispersion and L is the thickness of the material through which the beam propagates. The estimated pulse dispersion for a 106.4 fs pulse was 5 fs, which places the estimate within the error range of the recorded pulse width.

As previously mentioned, strong drift during the interferometric autocorrelation measurement necessitated active z-feedback to mitigate macroscopic drift. The drift became a factor since the measurement time for an entire autocorrelation trace was in the range of several minutes, depending on the measurement parameters. Partial segments of the trace were also measured and resolved with the minimal achievable delay step by executing a tip lift and then stepping the delay. This revealed the system's ability to resolve single oscillations of the autocorrelation trace with delay step sizes of 31 attoseconds. The capability to resolve the pattern on such a small timescale reinforces the hypothesis of this master thesis and of Schumacher et al. [6]

that the temporal resolution of nc-AFM is not limited by mechanical parameters, but only by the thermal limit. The minimal step size given in this particular measurement is determined by equation 3.5 and is composed of the minimal step size given by the delay stage upon which one of the silica wedges is mounted, on the other hand it is also influenced by the angular cut of the wedge pair and their refractive index. All of these parameters can be adjusted to allow for even smaller delay steps when combined with stable measurement conditions and sufficient averaging. Especially the use of wedge pairs with a lower refractive index as well as smaller angular cuts would significantly reduce the effective delay per distance driven where the minimal step interval of the underlying motor stage reaches its limit.

6 Conclusion and Outlook

In summary, this master thesis has seen the modification of an existing laser setup as presented by Schumacher et al. [6] and the incorporation of an optical intensity autocorrelator into the existing laser setup. The UHV AFM was outfitted with the capability to perform pump-probe measurements and interferometric autocorrelation measurements using the UHV AFM in conjunction with a Near Infrared Femtosecond Pulsed Laser.

The incorporated optical intensity autocorrelator allows for the characterization of NIR laser pulses, such as the determination of their pulse shape and width, as well as their relative delay. Furthermore, a physical delay mechanism consisting of a silica wedge pair was added to the laser setup in addition to the available delay stage, providing the system with a delay option which offers finer temporal resolution and delay. It should also be noted that the present laser setup, in contrast to its predecessor, is noncollinear both in regards to the optical intensity autocorrelator and the interferometric autocorrelator.

Using this setup, and specifically the optical intensity autocorrelator, the pulse shape and duration of the NIR laser were determined. The pulse shape was determined to possess a gaussian shape with a pulse duration of roughly 106 fs, contrasting the 94 fs, Sech2-shaped, pulse duration obtained by the manufacturer. By using the coarse delay line as a calibration aid, the fine delay was optimized to perform both optical intensity autocorrelation as well as interferometric autocorrelation, the latter of which was performed on a nonlinear Z-cut Lithium Niobate Crystal. The results from these interferometric autocorrelation measurements have both highlighted the capability of this system to perform pump-probe measurements with high temporal resolution, given a suitable sample, as well as reinforced the hypothesis by Schumacher et al. that nc-AFM is not intrinsically limited in its temporal resolution by mechanical constraints, but only by the thermal limit.

Furthermore, in resolving the interferometric autocorrelation trace, the experiments have demonstrated that pump-probe measurements aimed at detecting and measuring charge carriers and their lifetimes have a temporal detection limit which is only given by the pulse length of the laser used in the measurement.

The experiments performed for this master thesis have also demonstrated a remarkable minimal achievable delay time of 31.3 attoseconds, which is given by material parameters and can still be potentially improved. In many regards, this experimental series has been a proof of concept. Future projects may want to take advantage of the pulse-limited pump-probe time resolution in conjunction with the intrinsic spatial resolution of nc-AFM by investigating spatially confined electronic systems, such as quantum dots, as well as charge carriers with a lifetime close to the pump-probe laser's pulse length.

Acknowledgement

First and foremost, I wish to express my heartfelt gratitude and thanks to Prof. Peter Grütter for welcoming me in his research group and giving me the opportunity to complete my experiments at McGill University. I would also like to thank Prof. Ernst Meyer for acting as my supervisor and liaison to the University of Basel, as well as providing the context which gave me the opportunity to take the first steps towards this master thesis.

I also wish to express my gratitude to Zeno Schumacher, Rasa Rejali and Anreas Spielhofer for welcoming me in their basement UHV lab and introducing me to the various intricacies of UHV AFM.

I want to thank Zeno Schumacher specifically for providing endless, unwavering support, be it from proofreading and correcting my master thesis to helping with LabView programming and everything in between, as well as masterminding the general direction in which experimental efforts were directed.

I also wish to thank Rasa Rejali for introducing my to the UHV AFM in detail, as well as for her instrumental role in performing and refining measurements as well as sample preparation and transfer.

Next, I wish to thank Prof. David Cooke for providing crucial input concerning the autocorrelator setup and the choice of the nonlinear crystal, as well as for lending us essential parts of equipment such as the $\lambda/2$ waveplate, the BBo crystal, as well as the silica wedge pair and motor stage.

I furthermore wish to say thanks to the entire Grütter lab as well as my flatmate Kays Haddad for welcoming me and providing me with a wonderful, interesting and illuminating experience.

I wish to thank the Swiss Nanoscience Institute for awarding me one of their Argovia travel grants, which has greatly eased the financial aspect of an overseas semester.

Last but not least, I am also immensely grateful to my family and friends for keeping in frequent contact, and especially grateful to my girlfriend Tiziana for visiting me and keeping me company despite the distance!

Thank you all!

References

[1] G. Binnig, C. F. Quate, and C. Gerber, "Atomic Force Microscope," *Physical Review Letters*, vol. 56, pp. 930–933, mar 1986.

[2] G. Binnig and H. Rohrer, "Scanning tunneling microscopy," *Surface Science*, vol. 126, pp. 236–244, mar 1983.

[3] T. Glatzel, *Kelvin Probe Force Microscopy*, vol. 48 of *Springer Series in Surface Sciences*. Berlin, Heidelberg: Springer Berlin Heidelberg, 2012.

[4] R. García, "Dynamic atomic force microscopy methods," *Surface Science Reports*, vol. 47, pp. 197–301, sep 2002.

[5] T. R. Albrecht, P. Grütter, D. Horne, and D. Rugar, "Frequency modulation detection using high Q cantilevers for enhanced force microscope sensitivity," *Journal of Applied Physics*, vol. 69, pp. 668–673, jan 1991.

[6] Z. Schumacher, A. Spielhofer, Y. Miyahara, and P. Grutter, "The limit of time resolution in frequency modulation atomic force microscopy by a pump-probe approach," *Applied Physics Letters*, vol. 110, p. 053111, jan 2017.

[7] Z. Schumacher, "Time-domain Kelvin Probe Force Microscopy for Local Ultra-Fast Decay Time Measurements: PhD Thesis by Zeno Schumacher," 2016.

[8] F. J. Giessibl, "Forces and frequency shifts in atomic-resolution dynamic-force microscopy," *Physical Review B*, vol. 56, pp. 16010–16015, dec 1997.

[9] S. Mortia, R. Wiesendanger, and E. Meyer, *Noncontact Atomic Force Microscopy*, vol. 144. 2001.

[10] J. Israelachvili, *Intermolecular and Surface Forces*. Elsevier, 2011.

[11] I. Štich, J. Tóbik, R. Pérez, K. Terakura, and S. Ke, "Tip–surface interactions in noncontact atomic force microscopy on reactive surfaces," *Progress in Surface Science*, vol. 64, pp. 179–191, jun 2000.

[12] L. Zitzler, S. Herminghaus, and F. Mugele, "Capillary forces in tapping mode atomic force microscopy," *Physical Review B*, vol. 66, p. 155436, oct 2002.

[13] C. Rullière, *Femtosecond laser pulses*. 2005.

[14] R. Trebino, *Swamp Optics Tutorial Intensity Autocorrelation*. 2015.

[15] F. Kärtner, "Chapter 9: Pulse Characterization," in *UFOX lecture notes, ch. 9*, 2013.

[16] F. X. Kaertner, "Chapter 10 Pulse Characterization," *Ultrafast Optics*, vol. 1, pp. 333–370, 2005.

[17] Z. Schumacher, Y. Miyahara, A. Spielhofer, and P. Grutter, "Measurement of Surface Photovoltage by Atomic Force Microscopy under Pulsed Illumination," *Physical Review Applied*, vol. 5, p. 044018, apr 2016.

[18] M. Dood, "Second harmonic generation," *US Patent 4,910,740*, pp. 1–18, 1990.

[19] C. Kolmeder, W. Zinth, and W. Kaiser, "Second harmonic beam analysis, a sensitive technique to determine the duration of single ultrashort laser pulses," *Optics Communications*, vol. 30, pp. 453–457, sep 1979.

[20] G. C. Bhar, S. Das, and U. Chatterjee, "Noncollinear phase-matched second-harmonic generation in beta barium borate," *Applied Physics Letters*, vol. 54, no. 15, pp. 1383–1384, 1989.

[21] L. Howald, H. Rudin, and H. Güntherodt, "Piezoelectric inertial stepping motor with spherical rotor," *Review of Scientific Instruments*, vol. 63, pp. 3909–3912, aug 1992.

[22] R. S. Weis and T. K. Gaylord, "Lithium niobate: Summary of physical properties and crystal structure," *Applied Physics A Solids and Surfaces*, vol. 37, pp. 191–203, aug 1985.

[23] M. Bass, P. a. Franken, J. F. Ward, and G. Weinreich, "Optical Rectification," *Physical Review Letters*, vol. 9, pp. 446–448, dec 1962.

[24] F. Zernike and P. R. Berman, "Generation of Far Infrared as a Difference Frequency," *Physical Review Letters*, vol. 15, pp. 999–1001, dec 1965.

[25] K. Ravi, W. R. Huang, S. Carbajo, X. Wu, and F. Kärtner, "Limitations to THz generation by optical rectification using tilted pulse fronts," *Optics Express*, vol. 22, no. 17, p. 20239, 2014.

[26] F. Blanchard, X. Ropagnol, H. Hafez, H. Razavipour, M. Bolduc, R. Morandotti, T. Ozaki, and D. G. Cooke, "Effect of extreme pump pulse reshaping on intense terahertz emission in lithium niobate at multimilliJoule pump energies," *Optics Letters*, vol. 39, p. 4333, aug 2014.

[27] J. A. Fülöp, L. Pálfalvi, M. C. Hoffmann, and J. Hebling, "Towards generation of mJ-level ultrashort THz pulses by optical rectification," *Optics Express*, vol. 19, p. 15090, aug 2011.

[28] A. Rice, Y. Jin, X. F. Ma, X. Zhang, D. Bliss, J. Larkin, and M. Alexander, "Terahertz optical rectification from 110 zinc-blende crystals," *Applied Physics Letters*, vol. 64, pp. 1324–1326, mar 1994.

[29] Y.-S. Lee, N. Amer, and W. C. Hurlbut, "Terahertz pulse shaping via optical rectification in poled lithium niobate," *Applied Physics Letters*, vol. 82, pp. 170–172, jan 2003.

[30] P. A. Franken and J. F. Ward, "Optical Harmonics and Nonlinear Phenomena," *Reviews of Modern Physics*, vol. 35, pp. 23–39, jan 1963.

[31] I. Wilke and S. Sengupta, *Terahertz Spectroscopy*, vol. 20077041 of *Optical Science and Engineering*. CRC Press, dec 2007.

[32] S. Sanna and W. G. Schmidt, "Lithium niobate X -cut, y -cut, and Z -cut surfaces from ab initio theory," *Physical Review B - Condensed Matter and Materials Physics*, vol. 81, no. 21, pp. 1–11, 2010.

[33] W. Kinase, K. Ohi, K. Harada, H. Yagi, M. Inoue, M. Tashiro, S. Kashiwakura, H. Takei, and K. Nakamura, "Theory of optical property in LiNbO 3 . Elastooptic and electrooptic effects," *Ferroelectrics*, vol. 218, pp. 35–44, oct 1998.

[34] J. Dai and X.-C. Zhang, "Terahertz wave generation from gas plasma using a phase compensator with attosecond phase-control accuracy," *Applied Physics Letters*, vol. 94, p. 021117, jan 2009.

[35] S. T. Popescu, A. Petris, and V. I. Vlad, "Interferometric measurement of the pyroelectric coefficient in lithium niobate," *Journal of Applied Physics*, vol. 113, p. 043101, jan 2013.

[36] S. Grilli and P. Ferraro, "Dielectrophoretic trapping of suspended particles by selective pyroelectric effect in lithium niobate crystals," *Applied Physics Letters*, vol. 92, p. 232902, jun 2008.

[37] Q. Peng and R. E. Cohen, "Origin of Pyroelectricity in LiNbO3," *Physical Review B*, vol. 83, p. 220103, nov 2010.

[38] D. Irzhak, D. Roshchupkin, and D. Punegov, "Investigation of the Piezoelectric Effect in LiNbO 3 and LiTaO 3 Crystals by X-Ray Diffraction," *Ferroelectrics*, vol. 351, no. 1, pp. 163–175, 2007.

[39] M. Rosete-Aguilar, F. Estrada-Silva, N. Bruce, C. Roman-Moreno, and R. Ortega-Martinez, "Calculation of temporal spreading of ultrashort pulses propagating through optical glasses," *Revista mexicana de Fisica*, vol. 54, no. 2, pp. 141–148, 2008.

[40] I. H. Malitson, "Interspecimen Comparison of the Refractive Index of Fused Silica*,†," *Journal of the Optical Society of America*, vol. 55, p. 1205, oct 1965.

UNIVERSITÄT BASEL

PHILOSOPHISCH-NATURWISSENSCHAFTLICHE FAKULTÄT

Erklärung zur wissenschaftlichen Redlichkeit
(beinhaltet Erklärung zu Plagiat und Betrug)

Bachelorarbeit / Masterarbeit *(nicht Zutreffendes bitte streichen)*

Titel der Arbeit *(Druckschrift)*:

Femtosecond Time Resolution in FM-AFM by Incorporation of a Ultrafast Pulsed Laser System

Name, Vorname *(Druckschrift)*: Pachlatko, Raphael

Matrikelnummer: 12-055-190

Hiermit erkläre ich, dass mir bei der Abfassung dieser Arbeit nur die darin angegebene Hilfe zuteil wurde und dass ich sie nur mit den in der Arbeit angegebenen Hilfsmitteln verfasst habe.

Ich habe sämtliche verwendeten Quellen erwähnt und gemäss anerkannten wissenschaftlichen Regeln zitiert.

Diese Erklärung wird ergänzt durch eine separat abgeschlossene Vereinbarung bezüglich der Veröffentlichung oder öffentlichen Zugänglichkeit dieser Arbeit.

☒ ja ☐ nein

Ort, Datum: Montreal, 17. Juli

Unterschrift: R. Pachlatko

Dieses Blatt ist in die Bachelor- resp. Masterarbeit einzubinden.

UNI BASEL

7 Appendix

The dispersion calculation shown in equation 5.1 made use of multiple material constants which were retrieved from refractiveindex.info. The material components in the laser setup which generate dispersion consist of the two beam splitters, the $\lambda/2$ waveplate, the silica wedge pair, the window of the vacuum chamber and the focal lens for focussing the two beams onto the same spot below the cantilever tip.

All components save for the focal lens were made from fused silica, which possesses a group velocity dispersion of

$a_1 = 0.0189 \frac{fs^2}{\mu m}$,

according to Malitson [40], while the individual components have a combined thickness of

$$\begin{aligned} L_{fused\ silica} &= 2 * Beam\ Splitter * 45^\circ + 2 * Silica\ Wedge(avg.thickness) \\ &+ Chamber\ Window + \lambda/2 Waveplate \\ &= 11592 \mu m \end{aligned} \tag{7.1}$$

The focal lens itself is composed of two segments; the first segment is made of SF-5 glass with a GVD of

$a_2 = 0.06575 \frac{fs^2}{\mu m}$ and a thickness of 4 mm,

the second segment is made of N-SF6 HT glass with a GVD of

$a_3 = 0.10174 \frac{fs^2}{\mu m}$ and a thickness of 1.5 mm.

These parameters then substitute "aL" in equation 7.2:

$$\begin{aligned} \tau(L) &= \tau_0 \sqrt{1 + (\frac{8\ a\ L\ ln(2)}{\tau_0^2})^2} \\ &= \tau_0 \sqrt{1 + (\frac{8\ (L_{fused\ silica * a_1 + 4\ mm * a_2 + 1.5\ mm * a_3})\ ln(2)}{\tau_0^2})^2} \\ &= 111.4 fs \end{aligned} \tag{7.2}$$

where τ_0 is the gaussian pulse length of 106.4 fs obtained by the optical intensity autocorrelation.